< Submitted >

ROSAT X-RAY OBSERVATIONS OF THE RADIO GALAXY NGC 1316 (FORNAX A)

D.-W. Kim

Chungnam National University, Taejon, 305-764, South Korea; and

Harvard-Smithsonian Center for Astrophysics, 60 Garden Street, Cambridge, MA 02138

G. Fabbiano and G. Mackie[1]

Harvard-Smithsonian Center for Astrophysics, 60 Garden Street, Cambridge, MA 02138

February 20, 1997

1. Visiting Astronomer, Cerro Tololo Inter-American Observatory.

For the final report please see the following paper.

Abstract

We have observed NGC 1316 (Fornax A) with the ROSAT HRI. In this paper, we present the results of these observations and we complement them with the spectral analysis of the archival PSPC data. The spectral properties suggest the presence of a significant component of thermal X-ray emission ($> 60\%$), amounting to $\sim 10^9 M_\odot$ of hot ISM. Within $3'$ from the nucleus of NGC 1316, the HRI X-ray surface brightness falls as r^{-2} following the stellar light. In the inner $\sim 30''$, however, the X-ray surface brightness is significantly elongated, contrary to the distribution of stellar light, which is significantly rounder within $10''$. This again argues for a non-stellar origin of the X-ray emission. This flattened X-ray feature is suggestive of either the disk-like geometry of a rotating cooling flow and/or the presence of extended, elongated dark matter. By comparing the morphology of the X-ray emission with the distribution of optical dust patches, we find that the X-ray emission is significantly reduced at the locations where the dust patches are more pronounced, indicating that at least some of the X-ray photons are absorbed by the cold ISM. We also compare the distribution of the hot and cold ISM with that of the ionized gas, using recently obtained H_α CCD data. We find that the ionized gas is distributed roughly along the dust patches and follows the large scale X-ray distribution at r $> 1'$ from the nucleus. However, there is no one-to-one correspondence between ionized gas and hot gas. Both morphological relations and kinematics suggest different origins for hot and cold ISM. The radio jets in projection appear to pass perpendicularly through the central X-ray ellipsoid. Comparison of thermal and radio pressures suggests that the radio jets are confined by the surrounding hot gaseous medium.

1. INTRODUCTION

NGC 1316 (Fornax A, Arp 154) is a giant elliptical galaxy in the poor Fornax cluster. This galaxy exhibits many unusual features for an elliptical galaxy, including pronounced dust patches, H_α filaments, ripples and loops (e.g., Arp 1966; Schweizer 1980; Carter et al. 1983; Mackie and Fabbiano 1997). The distribution of the optical surface brightness reveals an extensive envelope, making NGC 1316 a typical D (or cD) galaxy (Schweizer 1980). It has one of the most pronounced shell systems observed in early type galaxies (Malin and Carter 1983). These features all point to a recent merging in NGC 1316 (e.g., Schweizer 1980).

In the radio (0.03 - 5 GHz), Fornax A is one of the brightest objects in the sky (L $= 2 \times 10^{42}$ erg sec^{-1}; Ekers et al. 1983). It contains giant radio lobes, separated by $\sim 30'$ ($\sim$240 kpc), consisting of polarized, organized filaments (Fomalont et al. 1989). A faint bridge between the lobes is displaced to the south of the galaxy center and S-shaped nuclear radio jets are present, implying a significantly violent action in the galaxy history, as also suggested by the optical data (e.g., Ekers et al. 1983; Geldzahler and Fomalont 1984). The nucleus of NGC 1316 hosts a low-luminosity AGN: optically it has a LINER-type spectrum (Veron-Cetti and Veron 1986; Baum, Heckman and van Breugel 1992); it contains a radio core (Geldzahler and Fomalont 1984); and HST observations have revealed a nuclear UV-bright point source (Fabbiano, Fassnacht and Trinchieri 1994b). NGC 1316 also contains complex, multiphase ISM: it has been detected in optical emission lines from ionized gas (e.g., Schweizer 1980; Phillips et al. 1986; Veron-Cetti and Veron 1986), IRAS far infrared emission (Knapp et al. 1989) and CO lines of molecular gas (Wiklind and Henkel 1989; Sage and Galletta 1993).

In X-rays, NGC 1316 was detected with Einstein (Fabbiano, Kim and Trinchieri 1992) and belongs to a group with the lowest L_X/L_B ratio among E and S0 galaxies (Kim, Fabbiano and Trinchieri 1992b). Therefore, based on the global amount of X-ray emission, NGC 1316 does not necessarily contain a large amount of hot ISM (see Fabbiano, Gioia and Trinchieri 1988). In this, it is similar to other galaxies which may have experienced recent mergers (Hibbard et al. 1994; Fabbiano and Schweizer 1995). ROSAT PSPC (Feigelson et al. 1995) and ASCA observations (Kaneda et al. 1995) have revealed the presence of extended Inverse Compton X-ray emission at the locations of radio lobes.

In this paper, we discuss the results of a re-analysis of the archival ROSAT PSPC observation of NGC 1316, and we report for the first time the results of high resolution X-ray observation with the ROSAT HRI. The HRI has ~5 arcsec resolution (David et al 1993), comparable to that of ground-based radio and optical data. With these data we establish the presence of a hot ISM in NGC 1316 and we correlate its properties to that of the other phases of the ISM. We also explore possible interactions between this hot ISM and the active radio nucleus.

This paper is structured as follows: in section 2, we present the results of the ROSAT HRI observation (§2.1 and §2.3) and the ROSAT PSPC data (§2.2); in section 3, we compare the X-ray data with the optical data, dust patches (§3.1) and ionized gas (§3.2); in section 4, we compare the X-ray results with the radio data; finally, in section 5 we discuss the implications of our results.

2. X-RAY OBSERVATIONS

NGC 1316 was observed with the ROSAT HRI on Jan. 14, 1994 and Jul. 7-10, 1994 for a total exposure time ~40 ks (3/4 of total observations were obtained in the July run). The two data sets are consistent with each other within the observational uncertainty. We present the combined results except as mentioned in §2.1. The field of view of this observation also includes the companion elliptical galaxy NGC 1317 (Figure 1). The observational log and basic parameters of both galaxies are given in Table 1. NGC 1316 was also observed with the ROSAT PSPC (Feigelson et al. 1995), and we used the PSPC archival data to determine spectral parameters.

Given the limited statistics of our HRI observation, we have used various binning and smoothing factors to investigate both large scale (a few arcmin) and small scale ($\lesssim$ 1 arcmin) features. We used both IRAF and software we developed ourselves to analyze our data. We adopt a distance to NGC 1316 of 27.2 Mpc using H_o = 50 km s^{-1} Mpc^{-1} (Fabbiano et al. 1992).

To extract source data, the field background must be subtracted. We found that estimates from the background map generated by the standard ROSAT SASS processing and from local measures of the background in concentric annuli around the sources agree well with each other. We will present results obtained with the local background subtraction.

2.1 X-ray Emission Features and Sources

The entire observed field of view is shown in Figure 1, where the X-ray contour map is overlaid on the optical image obtained from the Digitized Optical Survey[(2)]. The X-ray image was binned with a pixel size of 8″ and smoothed with a Gaussian of σ = 16″. The background is not subtracted. The octagonal shape indicates the boundary of the HRI detector. The figure shows a strong X-ray source at the center of the field, corresponding to the optical position of NGC 1316. Also X-ray emission is detected at the optical position of NGC 1317 (6.3$''$ to north of NGC 1316). Additionally, 10 point-like sources (above 3σ) are detected in the observed field. The source position, radius of the count extraction circle and X-ray count for each source are listed in order of RA in Table 2. The corresponding source numbers are marked in Figure 1. X-ray counts were extracted from circular regions centered on their X-ray centroids. The radius was determined with the radial profile of the X-ray surface brightness (§2.2.). Typically these radii extend to where the surface brightness is within ~3-4 % of the background. The background counts were extracted in annuli r=60$''$ - 200$''$, except for NGC 1316 where an annulus r=200$''$ - 400$''$ is used.

---

2. The Digitized Sky Survey was produced at the Space Telescope Science Institute under U.S. Government grant NAG W-2166. The images of these surveys are based on photographic data obtained using the Oschin Schmidt Telescope on Palomar Mountain and the UK Schmidt Telescope.

With the HRI observation of NGC 1316 we can trace the X-ray emission out to 170$''$, or 22.4 kpc at an adopted distance of 27.2 Mpc (see §2.2). However, the X-ray emission is extended at least to 1000$''$ (Fabbiano et al. 1992; Feigelson et al. 1995). The other sources (including NGC 1317) are point-like. Except for NGC 1316 and 1317, the sources are not identified with known objects in the SIMBAD catalog.

Source 2 and 12 are possibly variable. Their count rates from the two HRI observing epochs (Table 1) are significantly different (above 3 σ), while count rates of other sources are consistent within the count errors between the two observations (see Table 3). The small numbers of source counts do not warrant further temporal analysis.

The number of serendipitous sources (omitting the target galaxy) found in this observation is consistent with the expected number of background sources. According to the LogN-LogS function (Hasinger et al. 1993), we would have about 9 sources within a circular area of radius 15′ and a limiting flux 1.8×10^{-14} erg sec^{-1} cm^{-2} in 0.5-2.0 keV, which corresponds to the faintest among detected sources (Table 2) for a power law spectrum with $\alpha_E = 1$.

Figure 2 provides a close-up view of the NGC 1316 X-ray image which was binned with a pixel size of 2″ and smoothed with a Gaussian of $\sigma = 4''$, corresponding to FWHM = 11.3″ for an on-axis point source. This image covers a $3' \times 3'$ field which falls inside the optical galaxy ($12' \times 8.5'$ in $D_{25} \times d_{25}$; see Table 1). Inside the central arcmin, the X-ray emission is elongated along the NE-SW direction, following the optical major axis (PA=50°; RC3), while in a larger scale ($\sim 2'$), the X-ray emission is extended along the N-S direction. This extension is more pronounced toward the north (see also Figure 1).

In order to estimate whether the flattening of the X-ray isophotes at small radii is due to a real physical feature rather than chance positioning of a few noise 'blobs' from an underlying spherical distribution [as it would be expected from a gas in hydrostatic equilibrium with the stars (e.g., Buote and Canizares 1994)], we have run a Monte Carlo simulation. This involves: (1) choosing a spherical model; (2) creating a set of 'observations' in which Poisson noise is added to the model and each X-ray is distributed taking into account the HRI PRF; and (3) then determining the chance probability of occurrence of the observed features. We generated a smooth model image by adopting the X-ray radial profile determined in §2.2 under the assumption of spherical symmetry. This X-ray radial profile closely follows that of the optical surface brightness distribution (see §2.2). Then we normalized the model image and added background counts to match with our

HRI observation. We produced a set of 100 'observations' with a pixel size of 2″ (as in Figure 2) by estimating Poisson deviate for each pixel value and distributing the photon according to the PRF. To estimate how often we obtain an elliptical surface brightness by chance, we examined simulated images after smoothing with the same Gaussian σ as in Figure 2. Out of 100 images, no ellipticity as significant as that of Figure 2 is seen. In our simulations, we also added serendipitous sources at random positions according to the LogN-LogS function (Hasinger et al. 1993) to verify whether a few undetected point sources can mimic our observed features. However the results do not change appreciably. In conclusion, the chance probability to generate the observed, elongated distribution of the inner X-ray surface brightness out of a circularly symmetrical distribution is less than 1%.

To parameterize the X-ray surface brightness distribution, we have applied ellipse fitting to the image in Figure 2 (e.g., Jedrzejewski 1987), using the IRAF/STSDAS package. For a given semi-major axis, ellipse parameters (center of ellipse, PA of the major axis, ellipticity, etc.) are determined by an iterative method. The derived position angle and ellipticity are given in Figure 3a and b, where the ellipse parameters derived from the X-ray image seen in figs. 1 and 2 are plotted with crosses and open squares, respectively. These parameter are consistent with each other, except that in the inner region of the low resolution image (crosses) ϵ is smaller (i.e., the image is rounder) due to smoothing. We also derived the ellipse parameters using the PSPC image. The results are similar to those of the low resolution HRI image (crosses). The position angle of the major axis is almost constant ($\sim 50°$) at a $\lesssim 12''$, then after a short increase, reaches to PA $\simeq 0°$at a $\gtrsim 50''$. The ellipticity remains $\epsilon \simeq 0.3$ (0.2 - 0.4) in the whole radius range.

For comparison, we have also derived the optical ellipse parameters using the red continuum image obtained with a narrow band filter of λ_c=6693Å and FWHM=81Å (see §3.2 for optical observations). This red image was chosen because it is less affected by the dust absorption. While the position angle is almost constant at 50° in a = 2-200″ (small filled circles in Figure 3a), the optical ellipticity is smaller (i.e., the light distribution is rounder) than that of the X-ray image within a = 10″. At larger radii (a = 30-200″) the ellipticity becomes ~0.3, similar to the X-ray ellipticity (small filled circles in Figure 3b).

Figure 4 shows the central region in greater detail with a pixel size of 1″ and smoothed with a Gaussian of σ = 2″ which corresponds to an on-axis beam of 6.9″ FWHM. In this scale the core surface brightness divides into double peaks, separated by 7.3″. The optical center (RC3) is close (within arcsec) to the X-ray centroid determined with the image in Figure 2 and falls in the middle of the double peaks shown in Figure 4. Also noticeable are larger scale valleys at PA $\simeq$ 120° and PA $\simeq$ 320° which apparently bisect the core if extended to the center.

The double peaks and the SE-NW X-ray valleys are not caused by telescope aspect problems. We used only data obtained in the July run (see Table 1), to avoid a possible mismatch of the galaxy centers in the two observations due to aspect uncertainties, although source positions differ by less than 2″. The data obtained in the January run also present the same features but with larger statistical noise. To further check potential aspect problems, we applied the same binning and smoothing to point-like sources within the observed field. Sources 4, 7, and 8 which are within 5′ from the field center [therefore the HRI PRF is similar to the on-axis one (David et al. 1993)] are all circularly shaped while sources 2 and 12, both at 11′ off-axis distance (the PRF may not be circular), exhibit randomly elongated distribution.

The observed features are very interesting, because the radio jet (Geldzahler and Fomalont 1984) in projection appears to pass through the X-ray valleys (§4). However, the relatively low X-ray counts obtained in this high resolution image may produce an artificial feature by chance positioning of a few noise 'blobs'. To explore this possibility, we have rerun a Monte Carlo simulation as described above. Out of 100 simulations with a resolution same as Figure 4 ($1''$ pixel and $\sigma=2''$), 3 images exhibit double peaks and valleys, although not as significant as the observed. This simulation results imply that the existence of the double peaks and the X-ray valleys, although suggestive, is not conclusive and it is required to be confirmed by a deeper observation.

2.2 ROSAT PSPC Spectral Properties

In order to determine the X-ray spectral properties, we have used the ROSAT PSPC data obtained from the public archives. The method of data reduction is similar to that of the PSPC observations of NGC 507 (Kim and Fabbiano 1995). Because the X-ray emission is extended at least out to $1000''$ (see Feigelson et al. (1995) for discussions of the extended structure of X-ray emission), we determined the background at r=1800-$2400''$ and applied vignetting correction to each energy channel. Since we are interested in the galaxy emission, we have analyzed the X-ray emission within $180''$ from the center. Feigelson et al. (1995) found Inverse Compton (IC) radiation at the location of the extended radio lobes. The slope of the X-ray radial profile changes abruptly at r$\sim180''$, indicating that the X-ray emission in the central region has a different origin from that of the extended X-ray emission (Feigelson et al. 1995). To check for possible contribution of IC radiation to the X-ray emission within r $< 180''$, we also estimated the background using portions of the field within the PSPC support structure (r $\sim1000''$) where the diffuse emission is least. However, the results are not significantly different.

Using XSPEC, we found that the X-ray spectra within 180″ can be well reproduced either by a one-temperature, low abundance model (kT $\simeq$ 0.6-0.7 keV and ~10% solar abundance) or by a two-temperature, solar-abundance model ($kT_1 \simeq$ 0.1-0.2 keV and $kT_2 \simeq$ 0.8-0.9 keV at 90% confidence). In both cases, the acceptable range of N_H is consistent with the Galactic line-of-sight value (2×10^{20} cm^{-2}). The best fit parameters and acceptable ranges with N_H fixed at the line-of-sight value are listed in Table 4. Although we prefer the two-component model rather than almost zero-abundance model (see §5.1), both models suggest a significant amount of hot gaseous emission, because a significantly higher kT would be expected from a population of LMXB (see the analysis of the M31 bulge data by Fabbiano, Trinchieri and van Speybroeck 1987). We do not see any radial variations in the spectral parameters (temperature and N_H) with the PSPC observations (Table 4).

The absorption-corrected X-ray flux for the best fit parameters is 2×10^{-12} erg sec^{-1} cm^{-2} (see Table 5), corresponding to a X-ray luminosity of 1.8×10^{41} erg sec^{-1} at the adopted distance of 27.2 Mpc. The HRI flux is consistent with the *Einstein* IPC flux (see Table 1). For the two-component model, the X-ray flux of the very soft component is 30-40% of the total flux in 0.1-2.4 keV, similar to those seen in other X-ray faint early type galaxies (Fabbiano et al. 1994a, Fabbiano and Schweizer 1995).

To estimate the upper limits of hard X-ray emission from low-mass binaries as seen in the bulges of spirals (Fabbiano 1989) and in ellipticals (Matsushita et al. 1994), we added a 5 keV Bremsstrahlung component in the spectral fitting and determined the acceptable range of its normalization. The 90% upper limit of the hard component is 20% of the total flux in 0.1-2.4 keV for a one-temperature, low abundance model and 30% for a two-temperature, solar-abundance model. This upper limit corresponds to fluxes of $4-6\times10^{-13}$

erg $\sec^{-1}$ cm^{-2} and luminosities of $3-5\times10^{40}$ erg $\sec^{-1}$ (Table 5). The X-ray to optical luminosity ratio is then $L_X/L_B \leq 2-3\times10^{29}$ erg $\sec^{-1}$ $L_{\odot}{}^{-1}$ and is consistent with that of the bulge of M31 where X-ray emission is mainly from stellar sources. (e.g., Trinchieri and Fabbiano 1991).

2.3 Radial Profile

The PSPC spectral analysis suggests that > 60% of the NGC 1316 X-ray emission is from a hot gas component. Although with the present data is not possible to distinguish between this and other component of the emission, we will try in the following to constrain further the properties of the hot ISM from its average spatial properties.

Radial X-ray surface brightness profiles of elliptical galaxies can be used to estimate average gas parameters and can be compared with theoretical models (see e.g. review in Fabbiano 1989). Although our HRI data strongly suggest departures from a circularly symmetric distribution of the X-ray emitting gas in the central regions of NGC 1316, it is of some use to derive such a profile. To do so, we have ignored the central asymmetries, and we have derived a radial profile of the X-ray surface brightness measured in concentric rings centered on the NGC 1316 X-ray centroid (Table 2). The X-ray radial profile can be seen in Figure 5, where the raw, background and net counts are indicated by open squares, a solid line and filled squares, respectively. The emission is extended out to 170″, 22 kpc at the adopted distance of 27.2 Mpc. By subtracting a background level (the solid line in Figure 5) derived from r=200-400″, where no residual source emission can be detected, we produced the radial profile displayed in Figure 6. To this profile, we fitted a King approximation model, $\Sigma_X \sim (1+(\frac{r}{a})^2)^{-3\beta+0.5}$, convolved with the HRI point response function. In this equation, β is related to a true isothermal value by $\beta_i = 1.5\times\beta$ (e.g., Sarazin 1988). Best-fit model, fit residuals, and confidence contours are also shown in Figure 6. The best fit parameters and 90% confidence range with 2 interesting parameters (in parentheses) are: core radius a = 4.1″ (3.1–5.0″) and slope β = 0.51 (0.49–0.54), yielding χ^2 = 14.8 for 9 degrees of freedom. The estimated slope corresponds to $\Sigma_X \sim r^{-2.06\,(1.94-2.24)}$ for $r >> a$. This is close to that of the optical brightness distribution. Using the data in Schweizer (1981), we estimated the slope of the V_4 (5300-6400Å) surface brightness in r = 30″ to 300″ to be 2.02 ± 0.06. The radial slope measured with the red continuum image (§3.2) does not differ sinificantly. We also used the PSPC data to derive the radial profile of the X-ray surface brightness. Using the radial profile within r=180″ (to minimize the contribution of extended IC emission; see §2.3 and Feigelson et al. 1995), and a background count rate estimated at r=1800-2400″ (with vignetting correction), we find $\Sigma_X \sim r^{-2.25\,(2.12-2.45)}$, consistent with the HRI profile.

A central point source that may be the X-ray counterpart of the radio AGN was not detected with our HRI observations (see the HRI PRF indicated as a dashed line in Figure 5; see also Figure 4). To estimate an upper limit to a central point source, we applied the King model plus the HRI point spread function in fitting the radial profile and determined how strong a central source can be added without having χ^2 too large. We derive an upper limit (90%) for the central source of about 5% of the total counts, which corresponds to a flux of 1.0×10^{-13} erg sec^{-1} cm^{-2} in 0.1-2.4 keV and a luminosity of 9×10^{39} erg sec^{-1}. Here we assumed a power law with an energy index α_E=0.7 and line-of-sight N_H.

To derive the 3-dimensional density distribution, we have used a direct deprojection method (Kriss, Cioffi and Canizares 1983), where the emissivity (or density) is inwardly measured by subtracting the contribution of successive spherical layers. We implicitly assume that the hot gas is homogeneous and that the physical status of the gas at a given radius can be represented by one temperature and density. The deprojected density profile is shown in Figure 7a. We have assumed T = 0.8 keV (§2.3). The density profile corresponding to β=0.51, i.e., $n_e \sim r^{-1.53}$ is also shown as a dashed line in the figure.

Using the deprojected density distribution, we estimate the cooling time and gas pressure as a function of radius (Figure 7b). The cooling time is given as $\tau_c = 1.5 \frac{nkT}{n_e n_H \Lambda}$, where n, n_e and n_H are the total particle density, electron density, and Hydrogen density, respectively and Λ is the cooling function. The constant is in the range of 1 to 2.5, depending on its definition (see Sarazin 1988). The cooling time in the center is $\sim 10^8$ years, much smaller than the Hubble time; it reaches 10^{10} years at $\sim 180''$. To estimate the cooling function, we assumed solar metal abundances. With the PSPC spectral data (§2.3), the metal abundances cannot be determined unambiguously (see also e.g., Trinchieri et al. 1994; Fabbiano et al. 1994a). The cooling time in the central region is still much shorter than the Hubble time even with a zero metal abundance model. We also estimate the thermal gas pressure using the measured density and assuming kT = 0.8 keV (Figure 8).

We point out that these radial dependences of density, cooling time and pressure are only indicative average values. Because of the complexity of the surface brightness distribution in the inner regions, we would expect a range of these physical parameters at each radius, reflecting the clumpiness of the hot ISM. Also as remarked earlier, we cannot study separately the properties of the different components of the emission suggested by the PSPC data.

3. COMPARISON WITH OPTICAL DATA

3.1. Dust Patches

A detailed optical study of NGC 1316 by Schweizer (1980) and Carter et al. (1983) revealed many structures in this galaxy. There are several pronounced loops, ripples and dust lanes, all indicating recent mergers and infalls. The dust lanes are patchy, but the majority of the dust lies preferentially along the minor axis.

Figure 9 shows the distribution of dust patches (Schweizer 1980) superposed on the X-ray image (same as Figure 2). In general, the hot and cold ISM are related in the sense that the X-ray emission is significantly reduced at the locations where the dust patches are more pronounced. For example, the X-ray dip at ($3^h\ 22^m\ 43^s$, -37° 12′ 50″) coincides with the position where two dust patches are crossing and a blob of X-ray emission at (41^s, 11′ 55″) is surrounded by the dust patches. If confirmed by more sensitive data, the X-ray valleys and double peaks seen in Figure 4 may also be related to the dust lanes. The X-ray double peaks at the center may result from the absorption by cold ISM because the SE dust lane continues to the center of the galaxy, or it may indicate that the hot ISM at the location of cold ISM has already been cooled and its emission is outside the ROSAT X-ray band. The central portion of the SE X-ray valley is also at the same position as the dust lane and it could then be explained by the dust absorption. However, there are regions where this anti-correlation does not hold. The dust lane is bending at r$\sim$5″ from the center and is further apart (continued toward PA=150°) from the SE X-ray valley (continued toward PA=120°) afterward. Moreover, the NW X-ray valley running from the middle of the double peaks (Figure 3) is not coincident with the dust patches running in similar directions from the center, even allowing for uncertainties in the registration of the X-ray and optical images. In particular, the NW X-ray valley is offset by $\sim$10″ from the dust patch, although they are running almost parallel.

3.2. Ionized Gas

Because the ionized gas may be originated from the cooling hot gas, the distribution of ionized gas provides further clues of the relationship between cold and hot ISM. Narrow-band CCD images were taken on the photometric night of 1994 November 11/12. The CTIO/University of Michigan Curtis Schmidt 0.6/0.9m telescope was used with a Thomson 1024x1024 CCD. Pixel size is 19μm square (1.835″) however vignetting limits the useable field size to about 30′. Total exposure times were 8100s each for the redshifted (v=1801 km/s) $H\alpha$ + [NII] (λ 6563 + $\lambda\lambda$ 6548,6583) emission line filter (λ_c = 6606Å , FWHM=76Å), and continuum filter (λ_c = 6693Å , FWHM=81Å). Bias and dark frames were taken. Flatfields were generated from twilight sky exposures. The spectrophotometric standard HZ 4 was used to calibrate the narrow band images based on AB magnitudes (Oke 1994, private communication). The adopted magnitudes were AB_{6606}=15.01 and AB_{6693}=14.81. The $H\alpha$ + [NII] image was derived by subtracting a scaled, sky subtracted continuum image from the sky subtracted emission line image. The adopted scaling was calculated from a linear least square fit to residuals of 25 field stars calculated from several scaling factors. The mean pixel value of the $H\alpha$ + [NII] image at large radii of the optical galaxy was also consistently near zero.

The distribution of ionized gas is shown in Figure 10, superposed on the X-ray image (same as Figure 2). The overall distribution of the ionized gas is similar to that of the dust, ie., aligned toward north-south, slightly turned to NW and SE (clockwise), as observed in other early type galaxies with cold ISM (Kim 1989). The peak of the northern blob ($40^s.5$, $11'.8$) falls in between the dust patches, likely due to dust absorption. The eastern part of the southern blob generally follows the distribution of the dust patch.

Comparing the distributions of hot and warm ISM, we also find an overall similarity (e.g., N-S extension), but there is not always a one-to-one correspondence. Some features of the ionized gas appear to be related with the hot gas, while others do not. The southern extension of the ionized gas may be associated with the X-ray blob at (42s, 13′). Also the extended emission toward PA=50° from the southern peak and the E-W extension from the northern peak roughly follows the distribution of X-ray emission toward those directions. On the other hand, the peak of the northern blob ($40^s.5$, $11'.8$) coincides with the empty position of X-ray emission, surrounded by the X-ray emission.

4. COMPARISON WITH RADIO DATA

NGC 1316 (or Fornax A) contains large double radio lobes which are separated by $\sim$30′ (Wade 1961; Ekers et al. 1983). The circularly shaped lobes have polarized, organized filamentary structure (Fomalont, et al. 1989), but no hot spot is present in either side of the lobes. The center of NGC 1316 hosts a steep-spectrum core and two-sided jets ($\sim$30″) which are slightly S-shaped (Geldzahler and Fomalont 1984). The jets are not apparently connected with the radio lobes. A faint bridge between the two lobes is displaced to the south of the galaxy center (Ekers et al. 1983). These features imply a significant perturbation in the recent history of the galaxy as also suggested by the optical data (e.g., Ekers et al. 1983; Schweizer 1980).

Figure 11a shows the radio jets superposed on the X-ray image (same as Figure 2). This radio image was reproduced from the Figure 2b in Geldzahler and Fomalont (1984), which was obtained with the VLA and has 4″ resolution at 1.5 GHz. The direction of the radio jet is in projection perpendicular to the direction of NE-SW elongation of the central X-ray distribution. Geldzahler and Fomalont (1984) suggested that there may be interaction between dust patches and the radio jets. In some cases (e.g., Cen A; Kotanyi and Ekers 1979), the directions of radio jets and dust lanes are perpendicular, indicating such an interaction. However, in NGC 1316, the morphological correlation (the perpendicular nature) of the radio jets with the X-ray emission is much stronger than that with the dust patches.

If the existence of the double peaks and the X-ray valleys are confirmed, these may imply even more striking relations in that both sides of the radio jets in projection coincide with the X-ray valleys at PA$\simeq$120° and PA$\simeq$320° (Figure 11b). As discussed in §3.1, it is not likely that these X-ray valleys (possibly except the central portion of the SE X-ray valley) are totally due to absorption by cold ISM. This may suggests that the radio jets are interacting with the surrounding hot gaseous medium as seen in Cygnus A (Carilli, Perley and Harris 1994).

5. DISCUSSION

5.1 The Nature of X-ray Emission of NGC 1316

The X-ray emission of E and S0 galaxies can be due to different sources (see Fabbiano 1989): a hot gaseous halo dominating the emission in the X-ray bright early type galaxies; integrated stellar X-ray binary emission, seen in the bulges of spirals (see Fabbiano 1989) and confirmed in ellipticals with ASCA (Matsushita et al. 1994); a nuclear source, seen in bright radio galaxies (Fabbiano et al. 1984; Worrall and Birkinshaw 1994); and a very soft component, seen in X-ray-faint early type galaxies (Kim et al. 1992b; Fabbiano et al. 1994a; Kim et al. 1996) of debatable nature (e.g., Pellegrini and Fabbiano 1994). NGC 1316 is both an X-ray faint D (maybe cD) and a radio galaxy, therefore its X-ray emission is likely to be complex.

With the HRI imaging data and the PSPC spectral data, we can limit the contribution from the nuclear component and stellar binary component as being relatively unimportant. The upper limit to the nuclear X-ray emission obtained with the HRI image (§2.2) is $L_X \leq 9 \times 10^{39}$ erg sec^{-1}, which is about 5% of the total luminosity. With the PSPC spectra, we can pose an upper limit to the hard stellar component of 20-30% of the total flux in 0.1-2.4 keV ($L_X \leq 3-5 \times 10^{40}$ erg sec^{-1}; §2.3). This is consistent with the expected hard X-ray emission (e.g., scaling from the M31 bulge; Trinchieri and Fabbiano 1991).

The PSPC spectrum of NGC 1316 (§2.3) suggests that most of the X-ray emission within 3′ is due to a hot ISM in this galaxy. Although with the PSPC data we cannot unequivocally define the emission model, the spectral fits require the presence of a ~0.7-0.9 keV thermal emission (Table 4 and 5). The X-ray spectrum of NGC 1316 resembles that of other X-ray faint early type galaxies. X-ray spectra of those galaxies observed both with the IPC (Kim et al. 1992a) and the PSPC (e.g., Fabbiano et al. 1994a) present an excess of counts in the lowest energy channels, when compared to those of X-ray bright E and S0. This type of spectrum can either be fitted with a metal-free single-temperature optically-thin model, or with two (or more) component models (see Fabbiano et al. 1994a; Pellegrini and Fabbiano 1994; Fabbiano and Schweizer 1995). Recent ASCA measurements of the spectrum of the X-ray faint galaxy NGC 4382 (Kim et al. 1996) reject the single-component metal-free model in that galaxy, and by inference make it unlikely in X-ray faint galaxies in general. The two component model, in the case of NGC 1316, would consist of a very soft component of kT ~ 0.1-0.2 keV (which could be of stellar origin, e.g., Pellegrini and Fabbiano 1994), and a harder (kT ~ 0.7-1.0 keV), almost solar metallicity ISM. It is interesting that the abundance of the ISM determined from this two-component model is near to the optical metallicity of this galaxy (e.g., Gorgas, Efstathiou and Salamanca 1990). However, based on more general ASCA results on galaxies (e.g., Loewenstein et al. 1994; Arimoto et al. 1996), the latter may just be a coincidence.

Although a hot ISM is present, the total amount of hot gas is $\sim 10^9\ M_\odot$, only a fraction of that present in X-ray bright early type galaxies with a comparable optical luminosity (for example, $M_{gas} \sim 2 \times 10^{10}\ M_\odot$ in NGC 4636; Trinchieri et al. 1994). NGC 1316 clearly has not been accumulating all the gas ejected from the evolved stars during a Hubble time, which would be $\sim 3 \times 10^{10}\ M_\odot$. This is not surprising since this galaxy may have undergone recent merging events (see Schweizer 1980). Recent mergers (Hibbard et al. 1994) and dynamically young ellipticals (Fabbiano and Schweizer 1995) also tend to be relatively empty of hot ISM. It may be a coincidence, but the mass of the hot ISM is comparable with what would be expected from stellar accumulation in $\sim$1 Gyr, which may be the age of merger (Schweizer 1980). In a recent paper concerning with the optical and X-ray emission at larger radii, Mackie and Fabbiano (1997) find $\sim 3 \times 10^8\ M_\odot$ of hot ISM spatially coincident with the tidal tails in the outskirts of NGC 1316.

5.2 Disk formed in a rotating cooling flow?

We have found (§2.1) that the distribution of X-ray surface brightness is elongated (ellipticity ~ 0.3) along the optical major axis (PA $\simeq 50°$) within the central $\sim 30''$ ($\sim$4 kpc). This elongation significantly exceeds that of the stellar light particularly within $10''$ (§2.1). This geometrical information provides more evidence for a non-stellar origin of the X-ray emission in addition to the spectral argument (see §5.1). If the infalling cooling ISM carries angular momentum it may form an accretion disk, which could be extending out to a 10 kpc radius (see Kley and Mathews 1995; Brighenti and Mathews 1996). The NE-

SW flattened isophotes of NGC 1316 (Figure 2) may represent such a disk. Interestingly, this structure is approximately perpendicular to the radio jet of NGC 1316. Kley and Mathews (1995) note that radio jets may propagate preferentially along this direction (see also Begelman, Blandford and Rees 1984 for earlier work). They (see also Brighenti and Mathews 1996) also point out that the temperature profile expected in the presence of cooling disks would be more in agreement with the widespread central cooling in the ISM detected with ROSAT. The distribution of the X-ray surface brightness would also be less steep in the center in the presence of these disks than in the centrally accreting cooling flow case, and it may resemble that of the starlight, as observed in NGC 1316 (see §2.2).

An alternative possibility is that suggested in NGC 720 by Buote and Canizares (1994), where the elongated distribution of X-ray emission may in turn indicate the presence of extended, elongated dark matter if there is no rotational support. This is because the X-ray isophotes would be rounder than the optical isophotes for a hot gas in hydrostatic equilibrium with the stellar matter whose radial distribution is much steeper ($\sim r^{-3}$ for the stars compared with $\sim r^{-1.5}$ for the hot gas).

5.3 Multi-phase ISM

The comparison between X-ray and optical data reveals that the distribution of the X-ray emission is related with that of dust patches (§3.1.). The X-ray emission is weak where dust is seen and X-ray blobs are often surrounded by dust patches. The X-ray valleys running toward NW and SE from the center (Figure 4), if confirmed, may be real low density regions in the hot ISM, because they are not coincident with dust patches, except in the central SE region. The ionized gas is overall cospatial with the dust patches. However, the northern blob of the ionized gas falls in between dust patches, while the southern blob coexists with dust, indicating some of the line emission is absorbed by the dust.

The origin of the ionized gas (i.e., ionization mechanism) is unclear in early type galaxies. The emission lines often indicate LINER-type nuclear activity rather than HII regions, judged by for example the relative line strengths $H\alpha$ to [NII] flux ratio (e.g., Kim 1989). It has also been suggested that the gas is photo-ionized by post AGB stars (Trinchieri and di Serego Alighieri 1991). In the case of galaxies containing significant amounts of hot ISM, the ionized gas may also be the result of cooling flows (e.g., Sarazin 1988), but this is unlikely in NGC 1316.

In NGC 1316, the kinematics of the ionized gas revealed that the gas is rapidly (up to 350 km sec^{-1}) rotating along the minor axis (Schweizer 1980), while the stellar system rotates along the major axis (Bosma, Smith and Wellington 1985). The molecular gas also rotates along the minor axis (Sage and Galletta 1993). This suggests an external origin for the cold and ionized ISM, perhaps connected with the merging episode (Schweizer 1980; Mackie and Fabbiano 1997) and argues against the idea that the ionized/cold gas is originated from cooling hot gas. In the latter case both hot and cold/warm gas would be expected to have the same kinematics as the stars, since the hot ISM is likely to originate from stellar evolution. Different origins of warm gas (likely cold gas and dust as well) and hot gas may be further supported by our HRI observations in that the central X-ray flattening, possibly a disk (§5.2), would rotate along the major axis and that the morphological relationships between the ionized gas and the X-ray emission are lacking. Therefore, it is likely that the cold and warm ISM might be acquired externally by mergers and infalls occurred $\sim 10^9$ years ago, while the hot gas has been accumulated since the latest merger.

5.4 Is the radio jet thermally confined?

The possibility of thermal confinement is supported by the radial behaviour of the jet/ISM energetics. We estimated the radio jet pressure corresponding to the minimum energy using the radio map by Geldzahler and Fomalont (1984) (see Feigelson et al. 1995 for the validity of the minimum energy argument). We applied the prescription for a Gaussian jet given in Killeen, Bicknell and Ekers (1986a; see also Pacholczyk 1970). We also used the cylindrical jet approximation (see Perley, Willis and Scott 1979), but the results do not change significantly. We assumed that: the jet and the magnetic field are perpendicular to the line of sight; the energy of relativistic electrons is equal to that of protons and ions; the radio spectrum is a power law from 10 MHz to 10 GHz with a slope α=0.7; and the volume filling factor is unity. The estimated jet pressure is compared with the thermal pressure in Figure 8. At 6 - 24$''$ from the center, the jet pressure for both NW and SE jets is an order of magnitude lower than the thermal pressure. Radio and thermal pressure are supposed to be in balance in the case of thermal confinement. However, as discussed by Killeen et al. (1988) the radio minimum pressure could be easily underestimated (see also Pacholczyk 1970) while the similarity of the radial behaviour of radio and X-ray pressures argues for thermal confinement. This apparent contradiction between the thermal gas and minimum radio pressures has also been reported in similar cases where radio jets are expanding through the hot gaseous environment (e.g., Bohringer et al. 1993; Carilli, Perley and Harris 1994).

The possibility (suggested by Figure 8) that the jet is thermally confined inside a relatively small region reinforces the suggested lack of causal connection between the jet and the extended lobes (Ekers et al. 1983). It is possible that active events took place some time ago, probably induced by a merger ($\sim 10^9$ years ago; Schweizer 1980) and now the nucleus is relatively weak and the radio lobes are slowly cooling (see also Ekers et al. 1983). This idea is also supported by the relative power ($\sim$1/2500) of the jets to the extended radio lobes, which is a few hundred times lower than that of a typical early type galaxy (Slee et al. 1994); the lack of strong optical emission lines (see Schweizer 1980); the absence of a connection between the jet and the lobe (Geldzahler and Fomalont 1984); and the morphology of the lobes (Fomalont et al. 1989).

The double peaks and X-ray valleys seen in Figure 4, if confirmed, will provide more direct evidence for interaction between the hot gas and the radio jet. Both sides of the radio jets in projection appear to pass through the X-ray valleys which may play a role as nozzles in collimating the jets.

5.5 The Nucleus

Fabbiano et al. (1984) found a relationship between radio core power and X-ray luminosity in a sample of 3CR galaxies, indicating that both radio and X-ray emission are of non-thermal nuclear origin. This relationship holds down to radio faint galaxies (Fabbiano et al. 1989). Recently, with ROSAT observations, Worrall and Birkinshaw (1994) spatially decomposed central X-ray point sources from the diffuse, extended emission in several radio galaxies and confirmed the linear relationship between core radio and central X-ray emission in low-power radio galaxies. Although the X-ray core of NGC 1316 is not detected, the ratio between the X-ray upper limit (corresponding to $l_{1keV} \leq 6.3 \times 10^{21}$ erg s^{-1} Hz^{-1}) and the radio core emission ($l_{5GHz} = 2 \times 10^{28}$ erg s^{-1} Hz^{-1}, form Geldzahler and Fomalont 1984) is consistent with the linear relationship between these quantities discussed above.

A comparison of the spectral energy distribution (SED) of the NGC 1316 nucleus with those of other LINER galaxies can be found in Fabbiano and Juda (1997). It is worth noting the possible similarity between the nuclear sources of NGC 3998 and NGC 1316 (both early type galaxies). They both present a bright UV point-like source discovered with HST, and their SED differ from those of bright AGN (see also Fabbiano et al. 1994b). A better coverage of the nuclear emission of these faint AGN will be necessary to understand the emission mechanism.

6. CONCLUSION

We have presented the analysis of the high spatial resolution image and of the X-ray spectrum of NGC 1316 (Fornax A) obtained with the ROSAT HRI and PSPC. The results lead to the following conclusions:

(1) The X-ray spectrum of NGC 1316 ($r < 180''$) can be reproduced either by a single-temperature low-abundance model (kT = 0.7 keV and 10% solar) or by a two-temperature, solar-abundance model (kT_1 = 0.1-0.2 keV and kT_2 = 0.8-0.9 keV). These results indicate the presence of hot gaseous component contributing to >60% of the total X-ray emission. We set an upper limit of ~20% of the total emission due to a hard component from LMXB in NGC 1316, consistent with an extrapolation based on the bulge of M31. The total X-ray emission is 2×10^{41} erg sec^{-1} in the 0.1-2.4 keV band and $M_{gas} \sim 10^9 M_{\odot}$. The relatively small amount of hot ISM present in this X-ray faint galaxy [by comparison with that of X-ray bright E and S0 such as NGC 4636 and NGC 4472 (e.g., Fabbiano et al. 1992)] is consistent with observations of other systems that may have undergone relatively recent merging (Fabbiano and Schweizer 1995).

(2) The radial profile of the X-ray surface brightness falls as r^{-2}, which is close to the optical light distribution. No gradient of the X-ray emission temperature is seen.

(3) Within the central 30″, the X-ray isophotes are flattened along the optical major axis (they are significantly more flattened than the optical ones within 10″) and may represent an accretion disk formed in a rotating cooling flow. In a larger scale (1-2′), the X-ray emission is extended toward N-S, in agreement with the PSPC report of Inverse Compton emission (Feigelson et al. 1995).

(4) The X-ray emission is significantly reduced at the locations where the dust patches are more pronounced, indicating that some of the X-ray emission may be absorbed by the internal cold ISM in NGC 1316.

(5) The ionized gas is generally distributed along with the dust patches. Some features of the ionized gas appear to be related with a hot ISM but there is no one-to-one correspondence.

(6) Both morphological relations and kinematics suggest that the hot and cold/warm ISM may not have the same origin. The cold/warm ISM might be acquired externally by mergers/infalls, while the hot ISM has been accumulated since the latest merger.

(7) In projection, the direction of the radio jets is perpendicular to the central NW-SE elongation of the X-ray emission. The thermal pressure is higher than the jet equipartition pressure by an order of magnitude. However, the radial behaviour of thermal and radio pressures are similar, suggesting the possibility of thermal confinement.

(8) Although a nuclear source is not detected in X-rays, the upper limit ($L_X \leq 9 \times 10^{39}$ erg sec^{-1}) is consistent with the expectations, based on the extrapolation from low-power radio galaxies (Worrall and Birkinshaw 1994).

ACKNOWLEDGMENTS

This work was supported by NASA grant NAG 5-2152 (ROSAT), NAGW 2681 (LTSA), NASA contract NAS8-39073 (AXAF Science Center) and by Non Directed Research Fund, Korea Research Foundation. This research has made use of SIMBAD which is operated by the Centre de Donnees astronomiques de Strasbourg (CDS), France.

REFERENCES

Arimoto, N., Matsuchita, K., Ishimaru, Y., Ohashi, T., & Renzini, A. 1996 preprint

Arp, H. 1966, ApJS, 14, 1

Baum, S. A., Heckman, T. M. & van Breugel, W. 1992, ApJ, 389, 208

Begelman, M. C., Blandford, R. D., & Rees, M. J. 1984, Rev. Mod. Phys. 56, 255

Bohringer, H., Voges, W., Fabian, A. C., Edge, A. C., & Neumann, D. M. 1993, MNRAS, 264, L25

Bosma, A., Smith, R. M. & Wellington, K.J. 1985, MNRAS, 212, 301

Brighenti, & Mathews, W. 1996, preprint

Buote, D. A., & Canizares, C. R. 1994, ApJ, 427, 86.

Carilli, C. L., Perley, R. A., & Harris, D. E. 1994, MNRAS, 270, 173

Carter, D., Jorden, P.R., Thorne, D.J., Wall, J.V. & Straede, J.C. 1983 MNRAS, 205, 377

David, L. P., Harnden, F. R., Kearns, K. E., & Zombeck, M. V. 1993, The ROSAT High Resolution Imager (US ROSAT Science Data Center/SAO)

de Vaucouleurs, G., de Vaucouleurs, H., Corwin, H. G., Buta, R. J., Paturel, G., & Fouque, P. 1991 *Third Reference Catalogue of Bright Galaxies*, (**RC3**), (New York: Springer-Verlag)

Ekers, R. D., Gross, W. M., Wellington, K. J., Bosma, A., Smith, R. M., & Schweizer, F. 1983, AA, 127, 361

Fabbiano, G. 1989, ARAA, 27, 87

Fabbiano, G., Miller, L., Trinchieri, G., Longair, M., & Elvis, M. 1984, ApJ, 277, 115

Fabbiano, G., Gioia, I. M., & Trinchieri, G. 1988, ApJ,324,749

Fabbiano, G., Gioia, I. M., & Trinchieri, G. 1989, ApJ, 347, 127

Fabbiano, G., Kim, D.-W., & Trinchieri, G. 1992, ApJS, 80, 531

Fabbiano, G., Kim, D.-W., & Trinchieri, G. 1994a, ApJ, 429, 94

Fabbiano, G., Fassnacht, C., & Trinchieri, G., 1994b, ApJ, 434, 67

Fabbiano, G., & Schweizer, F. 1995, ApJ, 447, 572

Fabbiano, G., & Juda, G. 1997, in preparation.

Fabbiano, G., Trinchieri, G., and van Speybroeck, L. 1987, ApJ, 316, 127

Faber, S. M., and Gallagher, J. S. 1979, ARAA, 17, 135

Feigelson, E.D., Laurent-Muehleisen, S.A., Kollgaard, R.I., & Fomalont, E. B. 1995, ApJ, 449, L149

Fomalont, E. B., Ebnerter, K. A., van Breugel,J. M., & Ekers, R. D. 1989, ApJ, 346, L17

Geldzahler, B. J., & Fomalont, E. B. 1984, AJ, 89, 1650

Gorgas J., Efstathiou G. & Aragon Salamanca, A. 1990, MNRAS, 245, 217

Hasinger, G., Burg, R., Giacconi, R., Hartner, G., Schmidt, M., Trumper, J., & Zamorani, G. 1993, AA, 275, 1

Hibbard, J. E., Guhathakurta, P., van Gorkom, J. H., Schweizer, F. 1994, AJ, 107, 67

Jedrzejewski, R. I. 1987, MNRAS 226, 747

Kaneda, H., Tashiro, M., Ikebe, Y., Ishiski, Y., Kubo, H., Makishima, K., Ohashi, T., Saito, Y., Tabara, H., and Takahashi, T. 1995, ApJ, 453, L13

Killeen, N. E. B., Bicknell, G. V., & Ekers, R. D. 1986a, ApJ, 302, 306

Killeen, N. E. B., Bicknell, G. V., & Carter, D. 1986b, ApJ, 309, 45

Killeen, N. E. B., Bicknell, G. V., & Ekers, R. D. 1988, ApJ, 325, 180

Kim, D.-W. 1989, ApJ, 346, 653

Kim, D.-W., Fabbiano, G., & Trinchieri, G. 1992a, ApJS. 80, 645

Kim, D.-W., Fabbiano, G., & Trinchieri, G. 1992b, ApJ. 393, 134

Kim, D.-W., & Fabbiano, G., 1995, ApJ, 441, 182

Kim, D.-W., Fabbiano, G., Matsumoto, H, Koyama, K., & Trinchieri, G. 1996, ApJ, 468, 175.

Kley, W. & Mathews, W. 1995, ApJ, 438, 100

Knapp, G. R., Turner, E. L., & Cunniffe, P. E. 1985, AJ, 90, 454

Knapp, G. R., Guhathakurta, P., Kim, D.-W., & Jura, M. 1989, ApJS, 70, 329

Kotanyi, C. G. & Ekers, R. D. 1979, AA, 73, 1

Kriss, G. A., Cioffi, D. F., & Canizares, C. R. 1983, ApJ, 272, 439

Loewenstein, M., Mushotzky, R. F., Tamura, T., Ikebe, Y., Makishima, K., Matsushita, K., Awaki, H., & Serlemitsos, P. J. 1994, ApJ, 436, L75.

Mackie, G., & Fabbiano, G. 1997, AJ submitted

Malin, D. F., & Carter, D. 1983, ApJ, 274, 534

Matsushita, K., Makishima, K., Awaki, H., Canizares, C. R., Fabian, A. C., Fukazawa, Y., Loewinstein, M., Matsumoto, H. Mihara, T., Mushotzky, R. F., Ohashi, T., Ricker, G. R., Serlemitsos, P. J., Tsuru, T., Tsusaka, Y., & Yamazaki, T 1994, ApJ, 436, L41

Pacholczyk, A. G. 1970, *Radio Astrophysics* (San Francisco: Freeman)

Pellegrini, S. & Fabbiano, G. 1994, ApJ, 429, 105

Perley, R. A., Willis, A. G., & Scott, J. S. 1979, Nature, 281, 437

Phillips, M. M., Jenkins, C. R., Dopita, M. A., Sadler, E. M. & Binette, L. 1986, AJ, 91, 1062

Sage, L.J. & Galletta, G., 1993, ApJ, 419, 544

Sarazin, C. L. 1988 *X-ray emissions from clusters of galaxies* (Cambridge: Cambridge University press)

Schweizer, F., 1980, ApJ, 237, 303

Schweizer, F., 1981, ApJ, 246, 722

Slee O. B., Sadler E. M., Reynolds, J. E. & Ekers R.D. 1994, MNRAS, 269, 928

Trinchieri, G. & Fabbiano, G. 1991, ApJ, 382, 82

Trinchieri, G. & di Serego Alighieri, S. 1991, AJ, 101, 1647

Trinchieri, G., Kim, D.-W., Fabbiano, G. & Canizares, C. R. 1994, ApJ, 428, 555

Veron-Cetty, M. P. & Veron, P. 1986 , AAS, 66, 335

Wade, C. M. 1961, Pub. NRAO, 1, 99

Wiklind, T. & Henkel, C. 1989, AA, 225, 1

Worrall, D. M., & Birkinshaw, M. 1994, ApJ, 427, 134

Table 1

Basic parameters

	NGC 1316	NGC 1317
RA (J2000)[a]	3 22 41.6	3 22 44.7
DEC (J2000)[a]	-37 12 28	-37 6 10
B_T^o (mag)[a]	9.40	11.81
D (Mpc)[b]	27.2	27.2
D_{25} (arcsec)[a]	721	165
N_H (cm^{-2})[c]	2.0 x 10^{20}	2.0 x 10^{20}
HRI Observed Date[d]	Jan. 14, 1994	Jan. 14, 1994
HRI Exp time (sec)[d]	11038	11038
HRI Observed Date[e]	Jul. 7-10, 1994	Jul. 7-10, 1994
HRI Exp time (sec)[e]	29403	29403
PSPC Observed Date	Jan. 13-20, 1992	Jan. 13-20, 1992
PSPC Exp time (sec)	25500	25500
Log Fx (IPC) erg sec^{-1} cm^{-2}[f]	2.0 x 10^{-12}	<2.7 x 10^{-13}

a. Right Ascension (RA), declination (DEC), total face-on B magnitude (B_T^o), and major isophotal diameter measured at B = 25 magnitude $arcsec^{-2}$(D_{25}) taken from de Vaucouleurs et al. 1991 (RC3)

b. Distance from Fabbiano et al. 1992.

c. Galactic line of sight HI column density from Starks et al. 1992.

d. Sequence number 600255n00

e. Sequence number 600255a01

f. IPC flux from Fabbiano et al. 1992. Fluxes were estimated in a energy range of

0.2–4.0 keV for a Raymond-Smith model with solar abundance, kT=1keV and line of sight N_H. The count extraction radii are r=450″ for NGC 1316.

Table 2

X-ray sources

source number	X Y pixel	radius[c] arcsec	offaxis arcmin	vignetting correction	net cnts	error	Fx[e] 10^{-13}
1	5599.86 3823.70	30	12.9	1.076	67.44	15.77	0.53
2	5075.38 4998.42	25	10.9	1.055	89.45[d]	14.96	0.69
3	4468.47 4499.67	30	4.4	1.012	48.61	15.52	0.36
4	4104.82 3607.70	25	4.7	1.013	86.11	15.30	0.64
5[a]	4076.98 4108.50	170	—	—	2047.79	85.77	14.99
6[b]	4009.78 4862.26	20	6.2	1.020	120.29	15.05	0.90
7	3842.10 4436.98	25	3.4	1.008	35.52	13.19	0.26
8	3702.10 3687.70	30	5.1	1.015	68.92	16.08	0.51
9	3296.79 3583.91	15	8.1	1.033	31.89	9.79	0.24
10	3041.2 3157.04	25	12.0	1.065	53.90	13.76	0.42
11	2959.06 4396.66	20	9.7	1.045	44.42	11.83	0.34
12	2823.38 3703.22	20	11.2	1.057	201.14[d]	17.81	1.56

a. NGC 1316

b. NGC 1317

c. Background counts were extrated in annuli (r=200″- 400″ for NGC 1316; r=60″-200″ for all other sources).

d. variable (see Table 3).

e. Fluxes were estimated in a energy range of 0.1–2.4 keV for a Raymond-Smith model with solar abundance, $kT = 1$ keV and line of sight N_H. Vignetting correction was applied.

Table 3

Variable Sources

source	Jan. 94		Jul. 94		difference
number	rate	err	rate	err	σ
2	-0.47	0.56	3.22	0.46	5.09
12	7.81	1.04	3.92	0.46	3.41

Rates and errors are in unit of counts in 1,000 seconds.

Table 4

SPECTRAL FIT OF PSPC DATA[a]

2-Component fit with solar abundance[b]

radius ($''$)	kT_1 (keV)	kT_2 (keV)	Norm[c]	χ^2	degrees of freedom
0-60	0.16 (0.13-0.20)	0.83 (0.76-0.90)	1.68 (1.44-1.88)	26.61	23
60-180	0.15 (0.11-0.17)	0.86 (0.72-1.04)	0.74 (0.54-1.03)	17.89	23
0-180	0.16 (0.14-0.17)	0.84 (0.79-0.89)	1.23 (1.08-1.38)	25.34	23

1-component fit with varying abundance[d]

radius ($''$)	kT (keV)	Abundance (solar)	χ^2	degrees of freedom
0-60	0.70 (0.65-0.77)	0.12 (0.10-0.15)	11.36	24
60-180	0.59 (0.48-0.70)	0.03 (0.02-0.05)	21.14	24
0-180	0.68 (0.63-0.73)	0.08 (0.06-0.10)	12.99	24

a. N_H is fixed at the Galactic line-of-sight value, 2×10^{20} cm^{-2}.

b. Errors are at 90% confidence with 3 interesting parameters.

c. Normalization of the second component relative to the first component.

d. Errors are at 90% confidence with 2 interesting parameters.

Table 5

X-RAY FLUX AND LUMINOSITY[a]

	Flux[b]	Luminosity[c]
1-component model		
total	$1.9(\pm0.2) \times 10^{-12}$	$1.7(\pm0.2) \times 10^{41}$
upper limit of hard binary component	3.8×10^{-13}	3.3×10^{40}
upper limit of nuclear component[d]	1.0×10^{-13}	8.9×10^{39}
2-component model		
total	$2.0(\pm0.2) \times 10^{-12}$	$1.8(\pm0.2) \times 10^{41}$
0.2 keV component	$8.1(\pm1.0) \times 10^{-13}$	$7.2(\pm0.9) \times 10^{40}$
0.8 keV component	$1.2(\pm0.1) \times 10^{-12}$	$1.1(\pm0.1) \times 10^{41}$
upper limit of hard binary component	6.0×10^{-13}	5.3×10^{40}
upper limit of nuclear component[d]	1.0×10^{-13}	8.9×10^{39}

a. The data with $r < 180''$ are used and the errors are based on the acceptable range of normalization at 90%

b. Absorption-corrected flux in unit of erg sec^{-1} cm^{-2} in 0.1-2.4 keV.

c. Distance = 27.2Mpc

d. Estimated from the HRI image

Figure Captions

Figure 1. The entire field of view of this HRI observation (NGC 1316 and NGC 1317). The X-ray contours are overlaid on the optical image obtained from the Digital Sky Survey. X-ray image is binned with a pixel size of 8 arcsec, background-subtracted and smoothed with a Gaussian of $\sigma = 16$ arcsec. The octagonal shape indicates the boundary of the HRI detector. The source numbers are ordered by an increasing RA (see Table 2). RA and Dec are in J2000.

Figure 2. A close-up view of the X-ray image (with a pixel size of $2''$ and a Gaussian σ of $4''$). The contours indicate isophotes at 5% to 95% of the peak with 8 steps. RA and Dec are in J2000.

Figure 3. (a) Position angles and (b) ellipticities determined by ellipse fitting to the images seen in Figure 1 (crosses), Figure 2 (squares). Also optical ellipse parameters are shown as small filled circles.

Figure 4. same as Figure 2 but with a pixel size of $1''$ and a Gaussian σ of $2''$. The data obtained only in the July run are used. The contours indicate isophotes at 6% to 85% of the peak with 8 steps.

Figure 5. Radial distribution of X-ray counts. Raw, background (determined at r=200–$400''$), and net counts are indicated by open squares, a solid line and filled squares with error bars.

Figure 6. Radial profile of X-ray surface brightness and best fit model prediction.

Figure 7. (a) Deprojected density and (b) cooling time as a function of radius. The density

profile corresponding to β=0.51 ($n_e \sim r^{-1.53}$) is shown as a dashed line.

Figure 8. Thermal gas pressure as a function of radius. The minimum radio pressure along the jets is also plotted with filled circles (the NW jet) and open circles (the SE jet).

Figure 9. Distribution of dust patches (from Schweizer 1980) overlaid onto the X-ray image (same as Figure 2).

Figure 10. Distribution of ionized gas overlaid onto the X-ray image. The continuum-subtracted $H\alpha$ + [NII] image was smoothed with a 2 pixel (full width) gaussian filter and the X-ray image is the same as Figure 2.

Figure 11. Radio jet overlaid onto the X-ray image. The radio map was taken from Geldzahler and Fomalont (1984). The X-ray image is the same as (a) Figure 2 and (b) Figure 4.

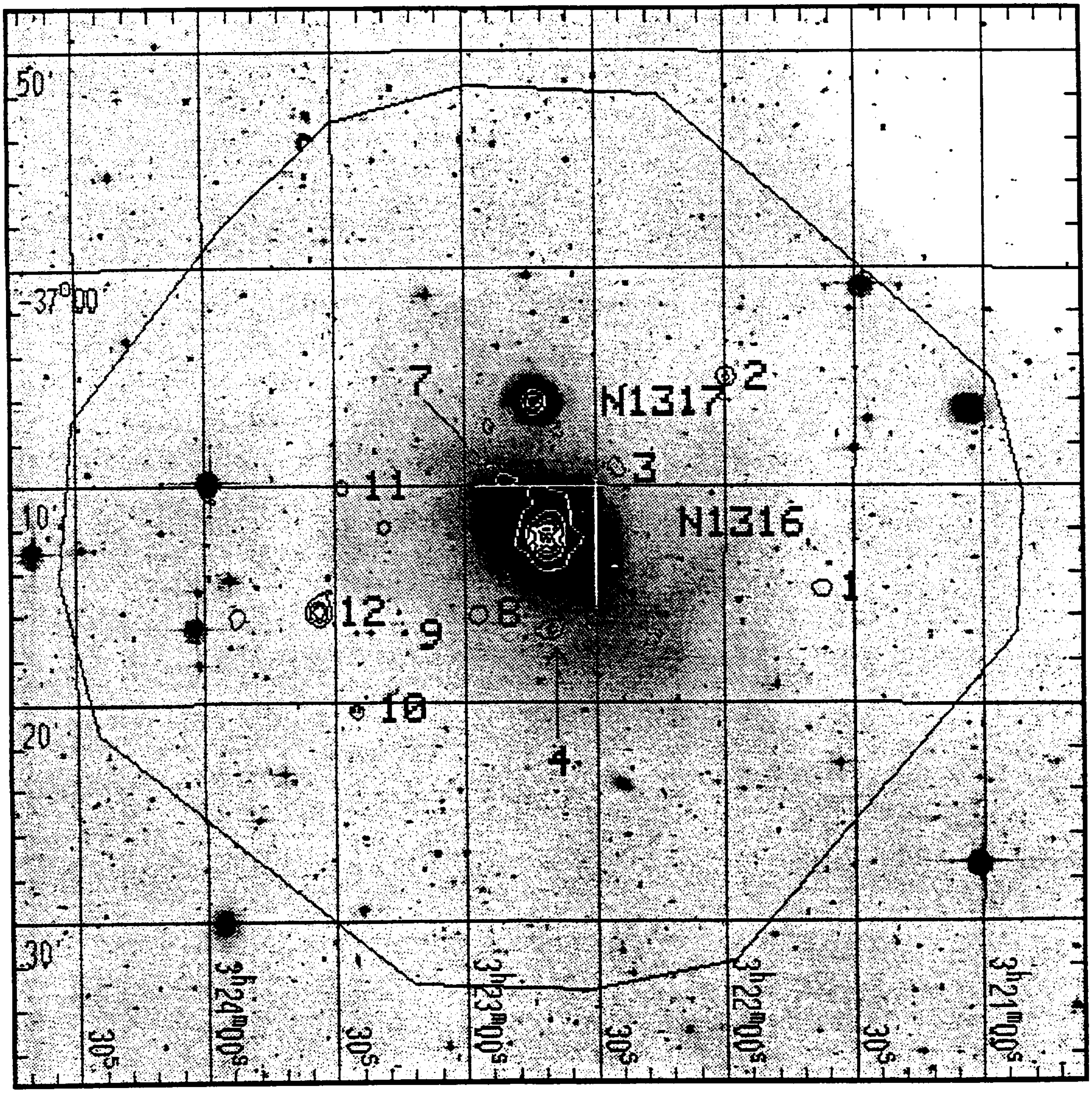

50'
-37°00'
10'
20'
30'
N1317
N1316
1
2
3
4
6
7
9
10
11
12
3h24m00s
3h23m00s
3h22m00s
3h21m00s
30s

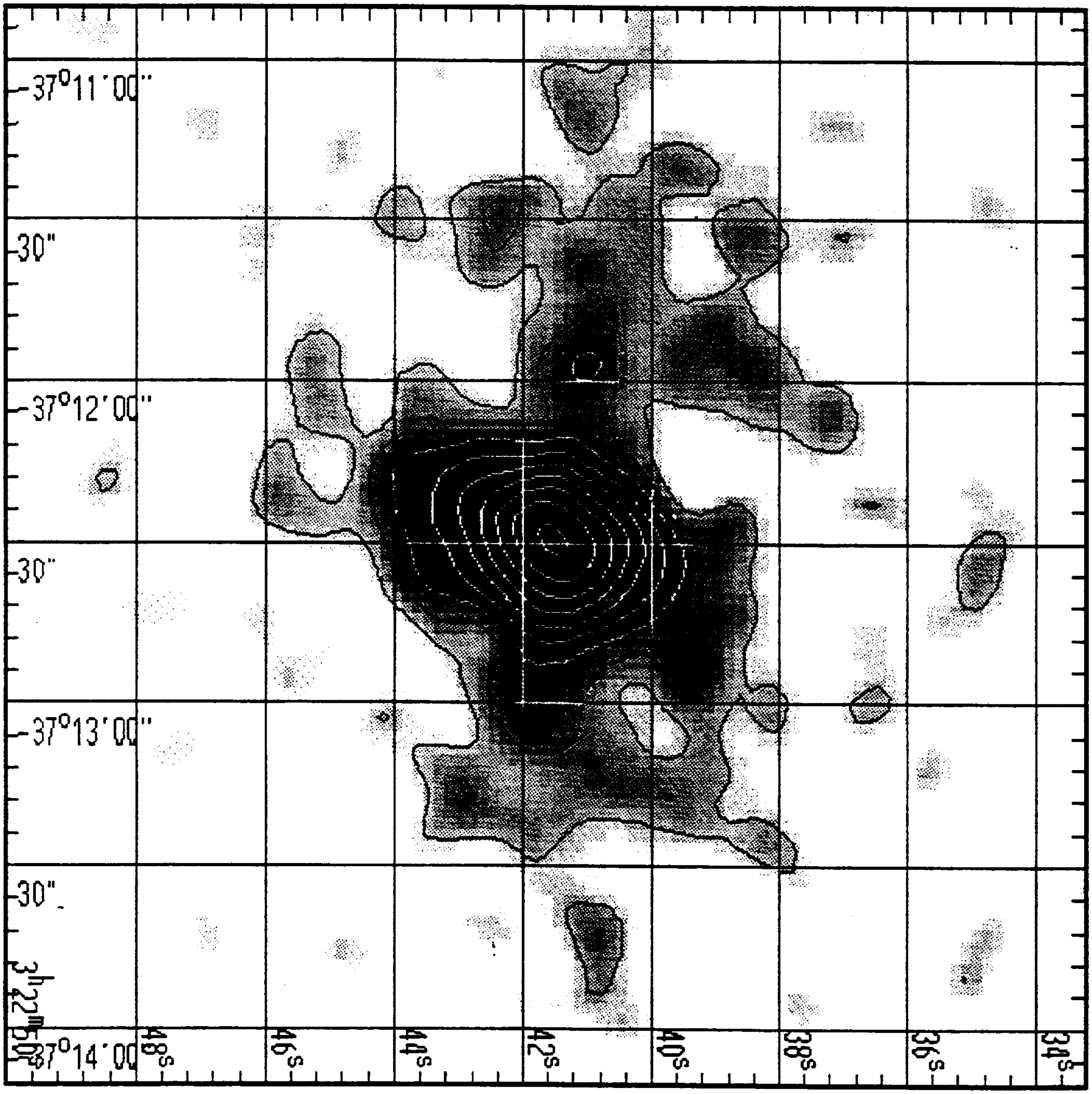

-37°11'00"
30"
-37°12'00"
30"
-37°13'00"
30"
-37°14'00"
3h22m50s
48s
46s
44s
42s
40s
38s
36s
34s

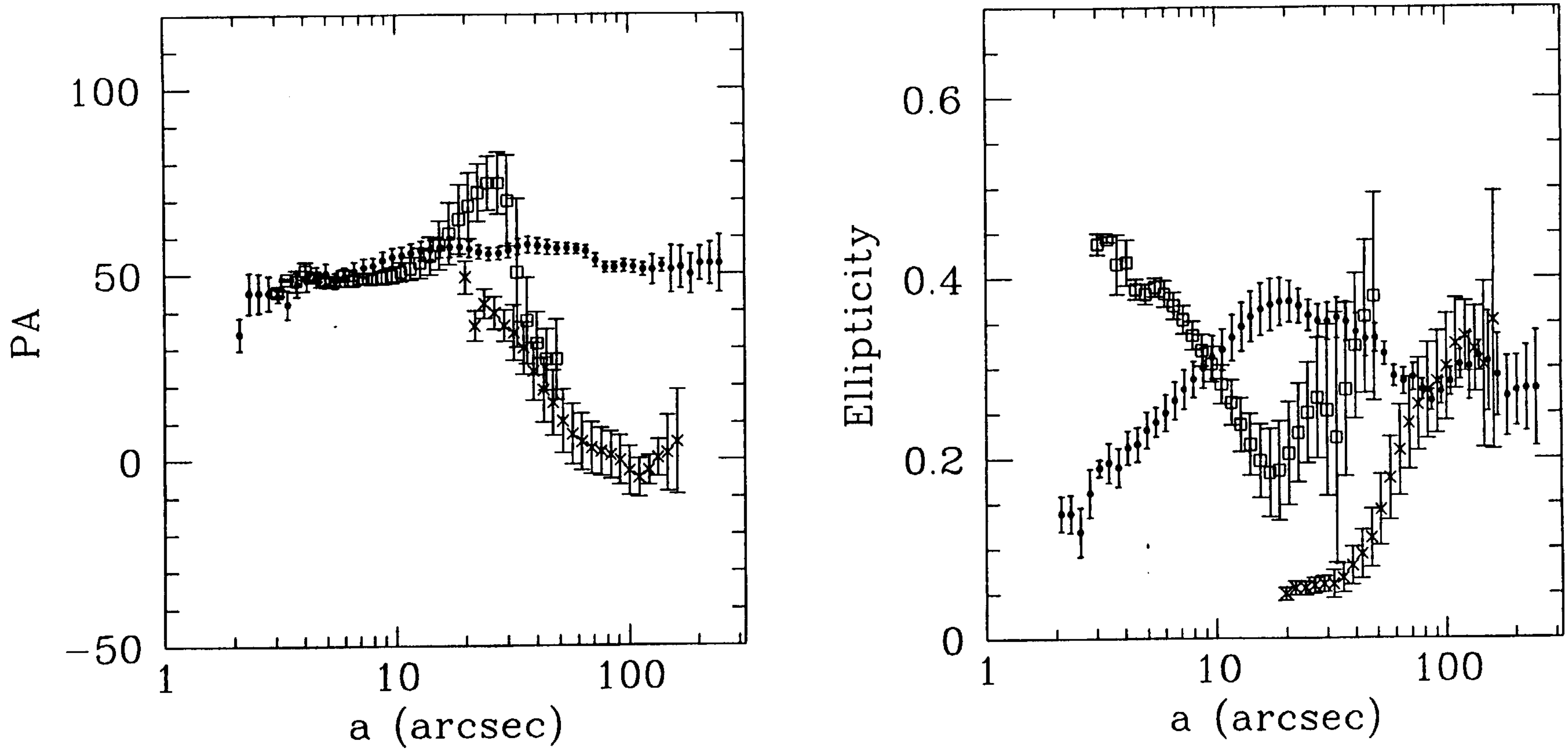
PA
100
50
0
−50
1
10
100
a (arcsec)
Ellipticity
0.6
0.4
0.2
0

N1316b

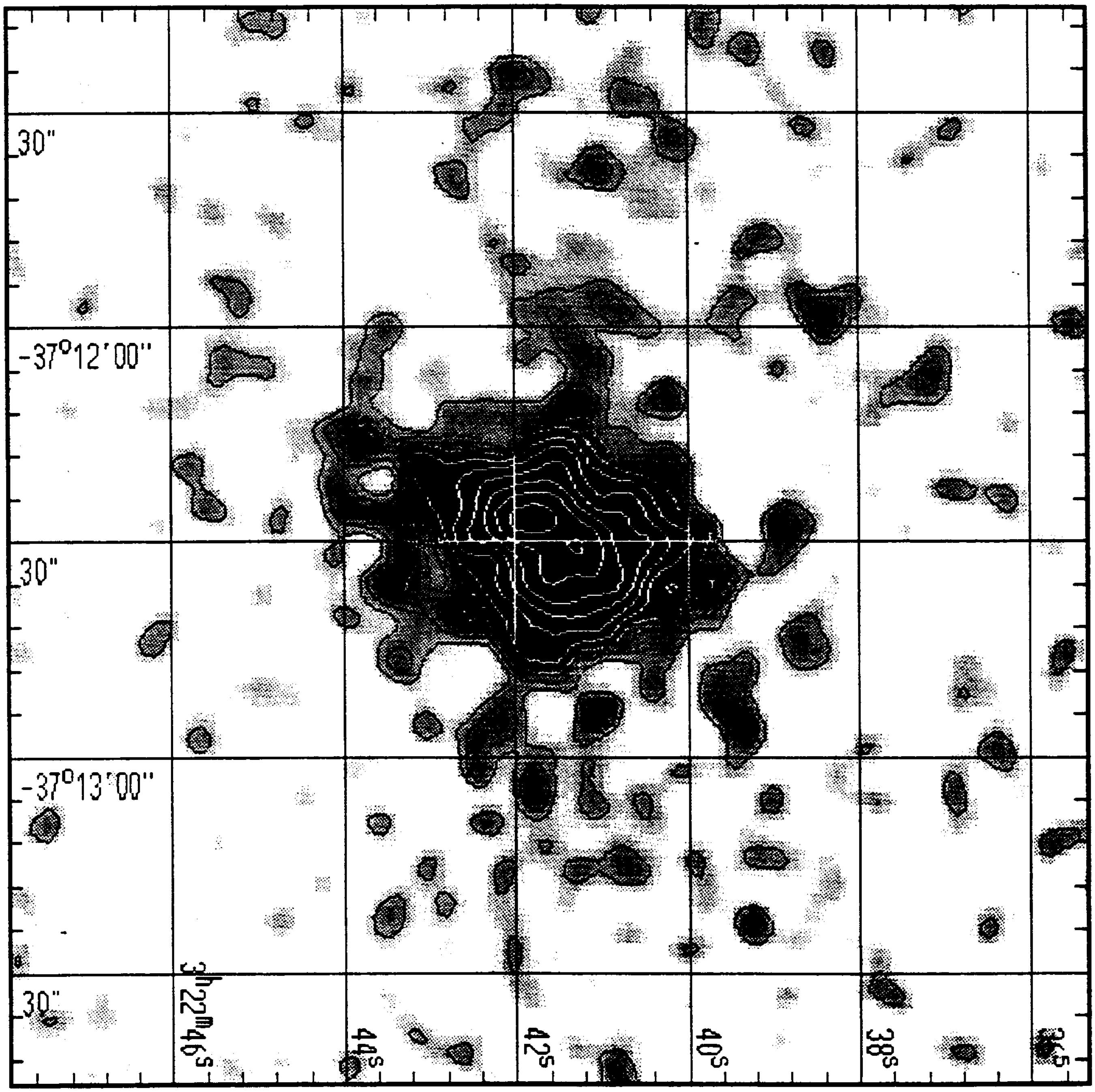

47

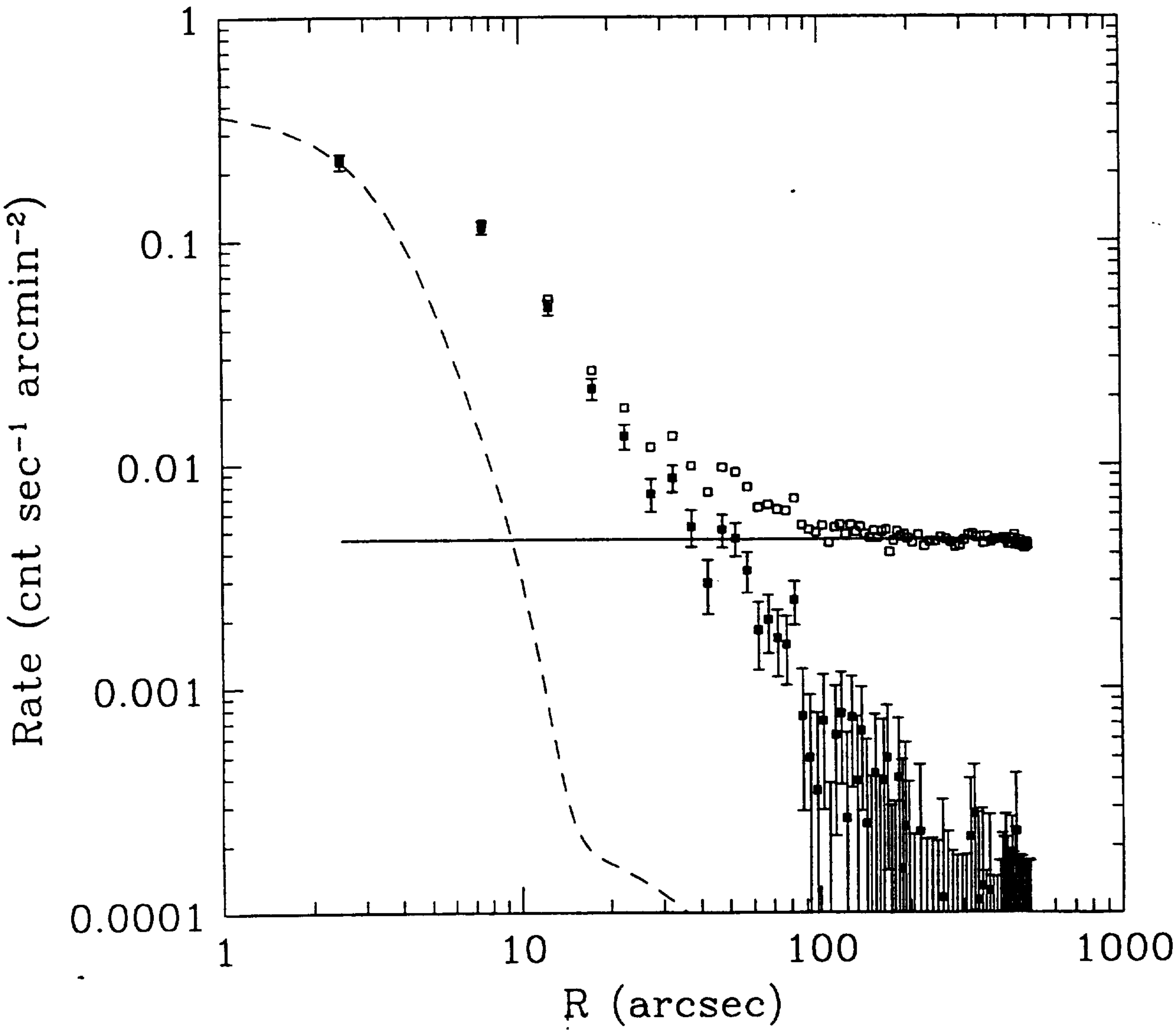

1
0.1
0.01
0.001
0.0001
Rate (cnt sec^{-1} arcmin^{-2})
1
10
100
1000
R (arcsec)

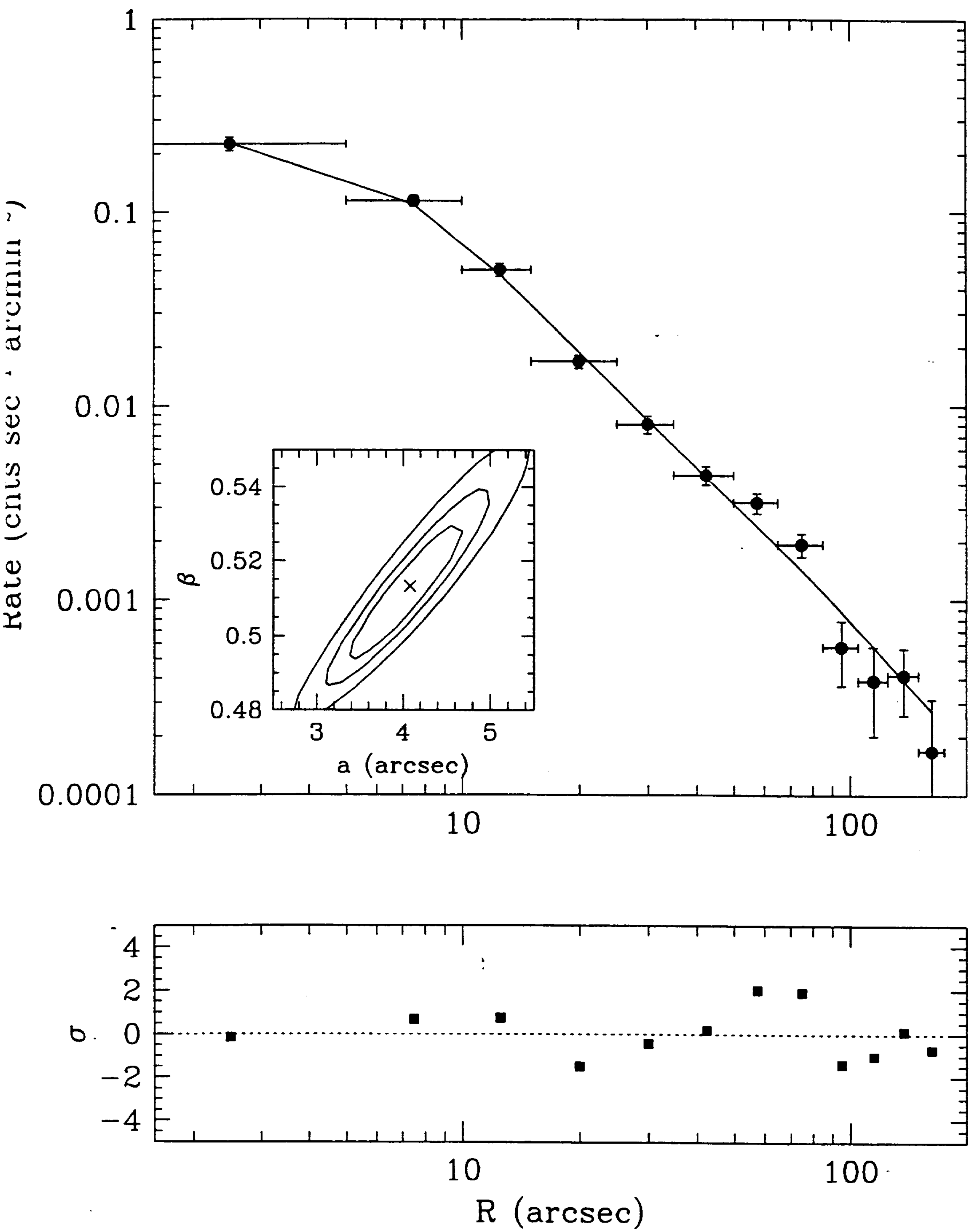

Rate (cnts sec arcmin
1
0.1
0.01
0.001
0.0001
10
100
β
0.54
0.52
0.5
0.48
3
4
5
a (arcsec)
σ
4
2
0
−2
−4
10
100
R (arcsec)

6

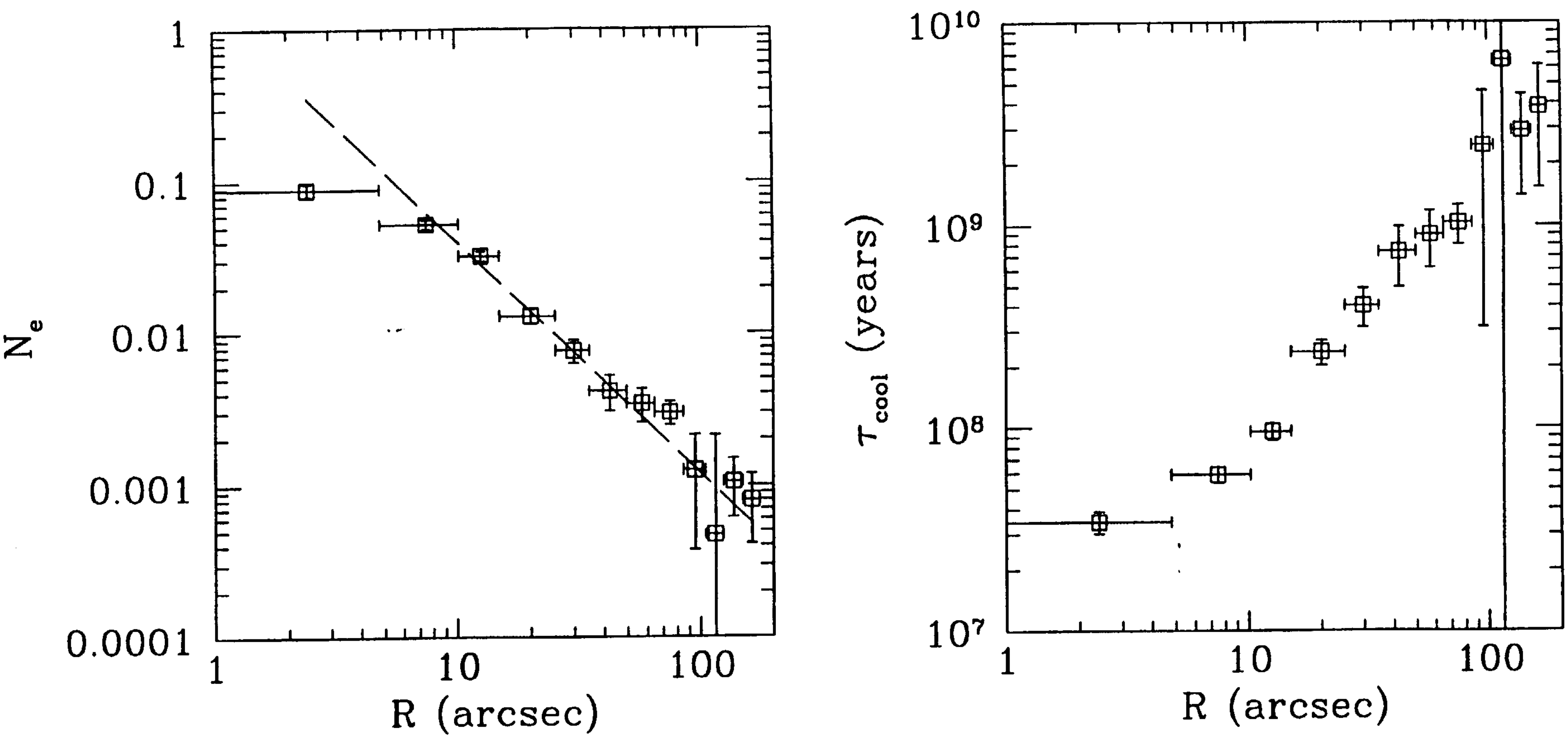

N_e
1
0.1
0.01
0.001
0.0001
1
10
100
R (arcsec)
τ_cool (years)
10^10
10^9
10^8
10^7
1
10
100
R (arcsec)

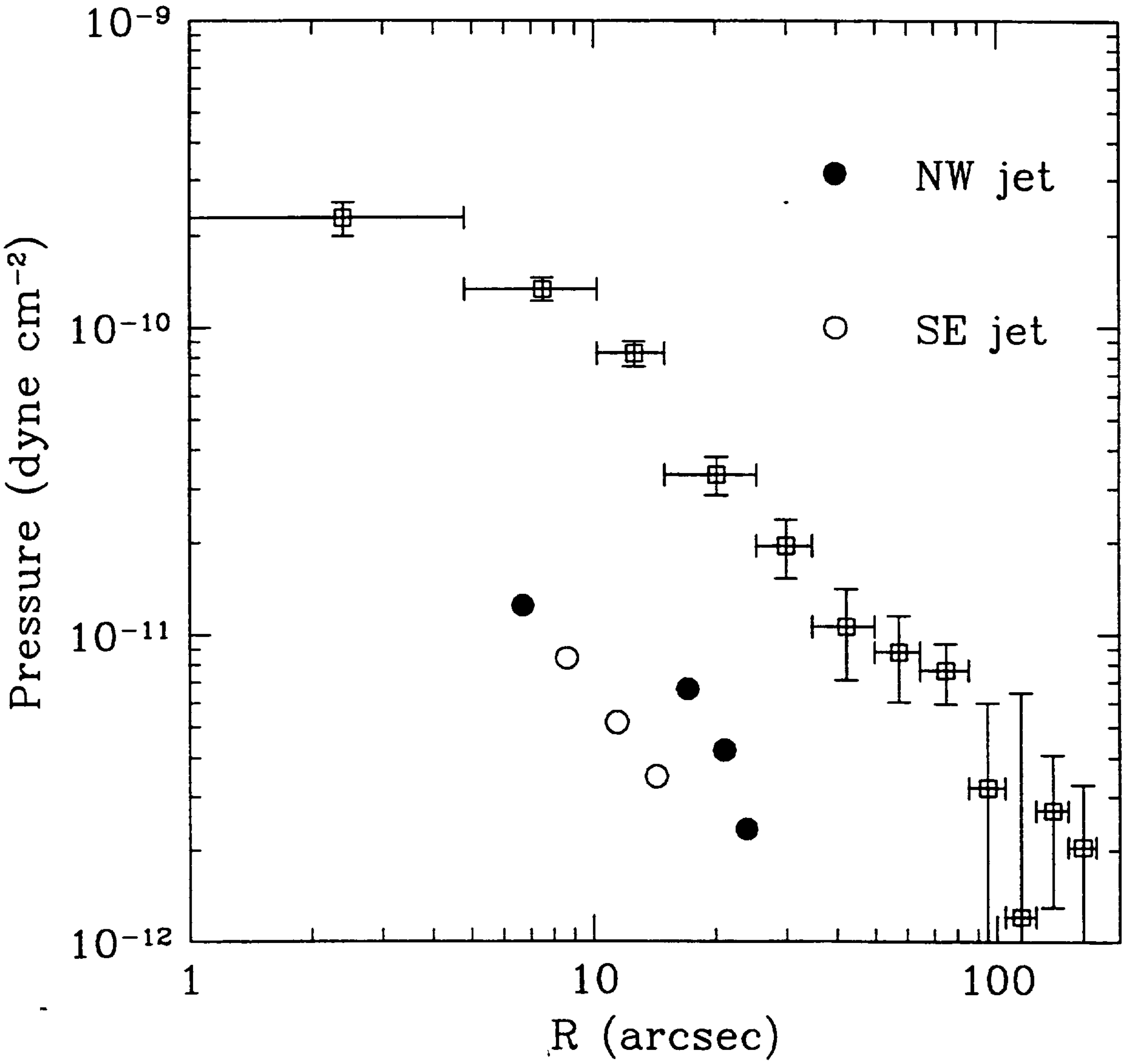

NW jet
SE jet
Pressure (dyne cm^{-2})
10^{-9}
10^{-10}
10^{-11}
10^{-12}
1
10
100
R (arcsec)

8

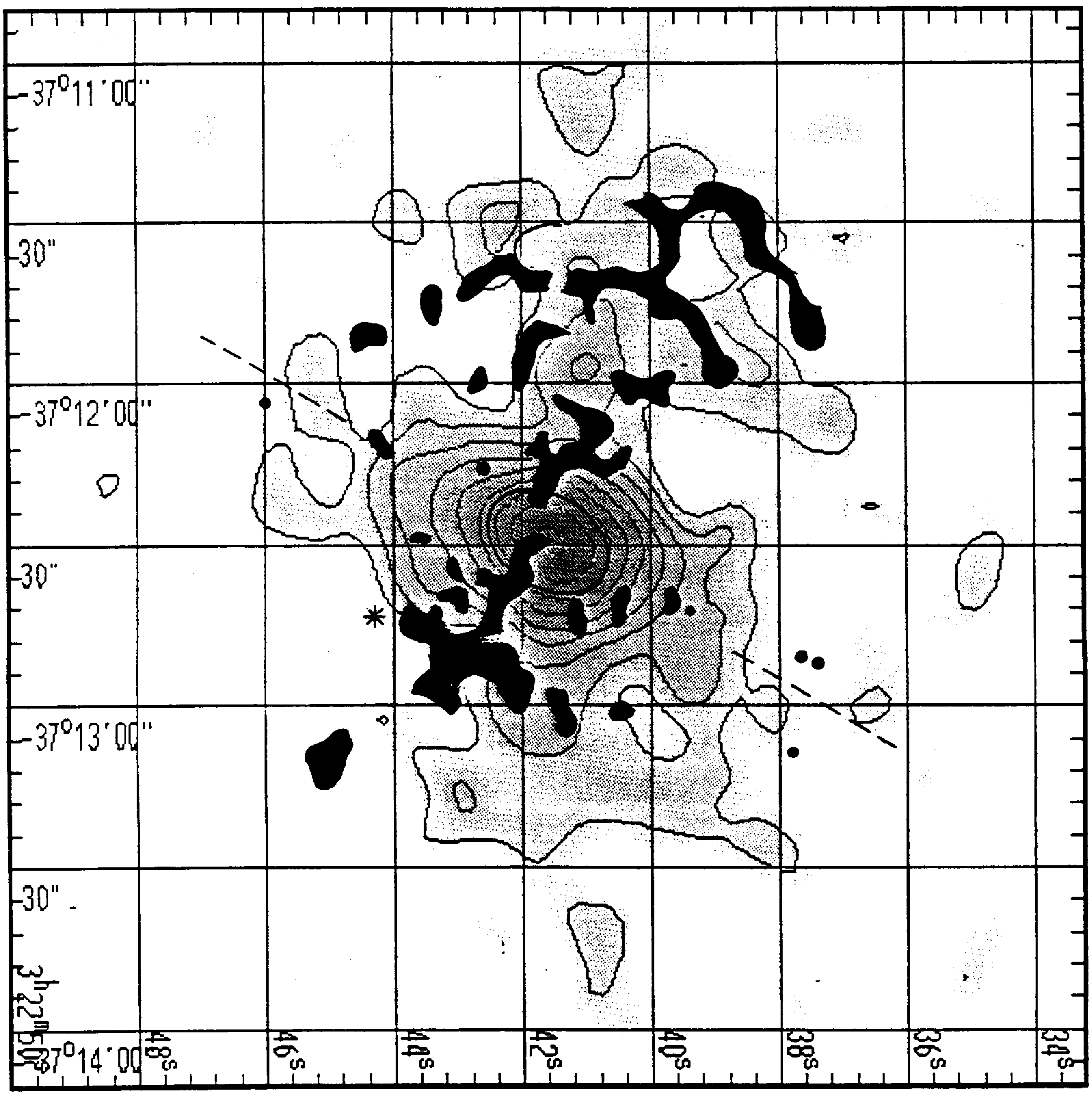
-37°11'00"
-30"
-37°12'00"
-30"
-37°13'00"
-30"
-37°14'00"
3h22m50s
48s
46s
44s
42s
40s
38s
36s
34s

fig 9

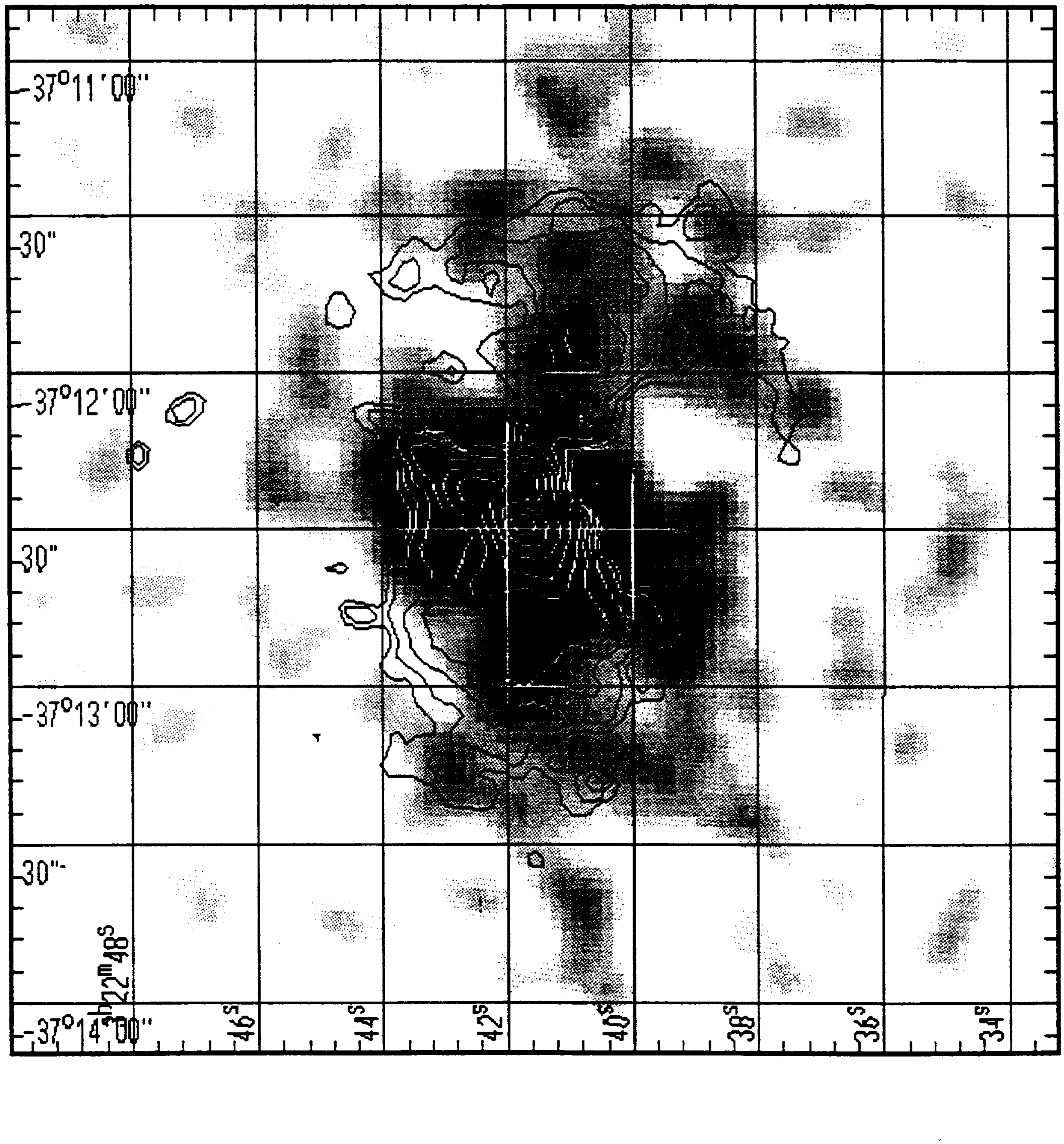

-37°11'00"
30"
-37°12'00"
30"
-37°13'00"
30"
-37°14'00"
3h22m48s
46s
44s
42s
40s
38s
36s
34s

10

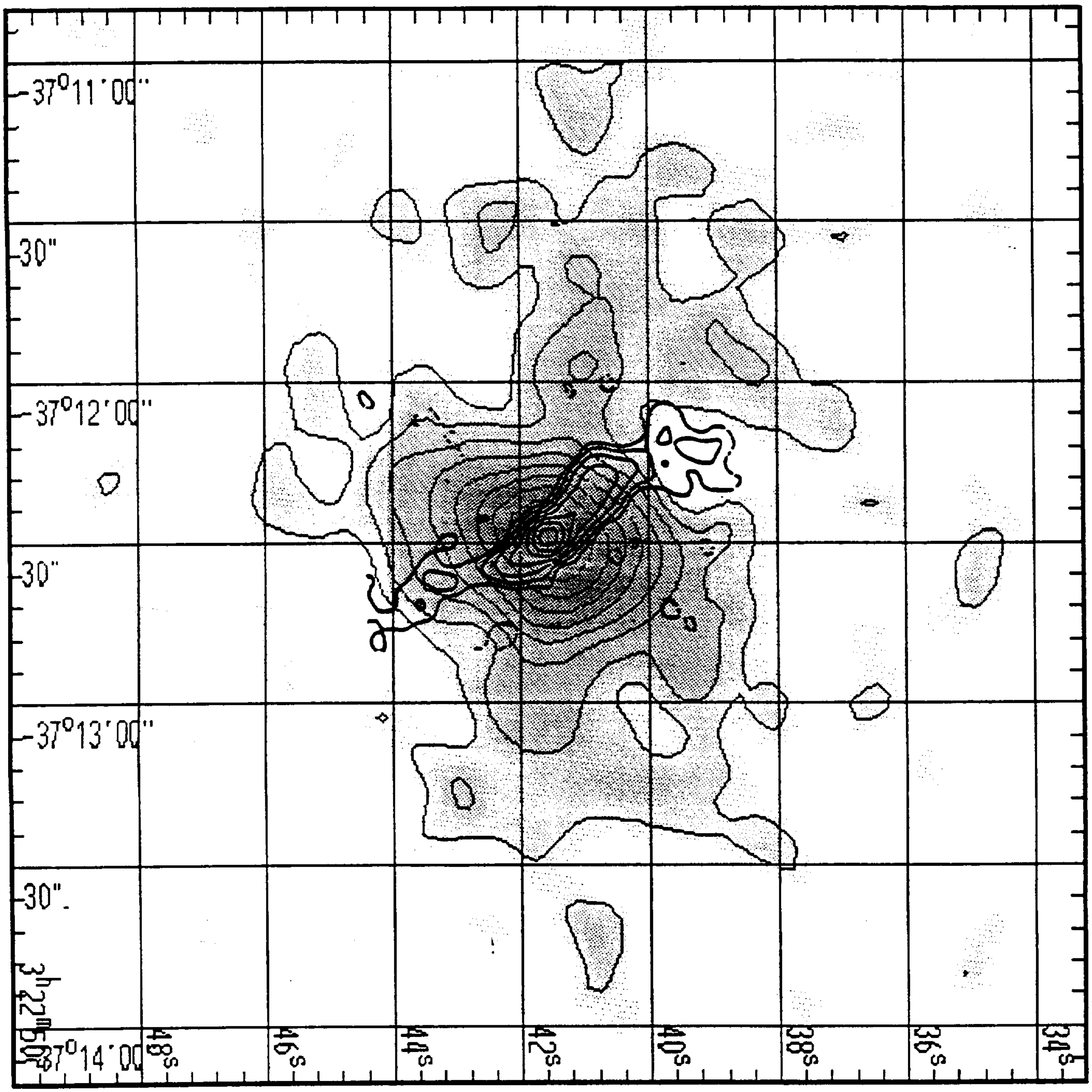

-37°11'00"
30"
-37°12'00"
30"
-37°13'00"
30"
-37°14'00"
3h22m50s
48s
46s
44s
42s
40s
38s
36s
34s

11

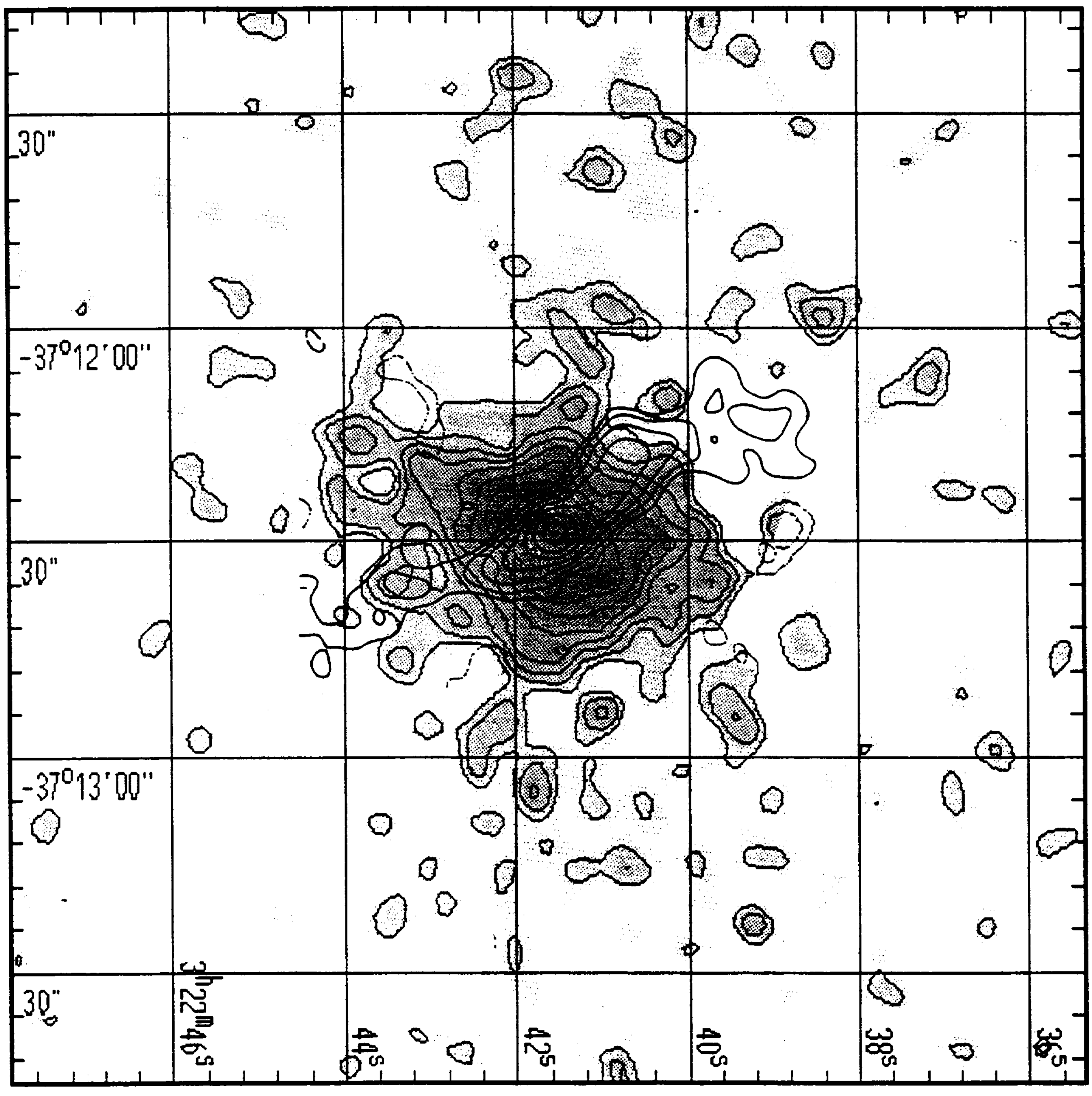
30"
-37°12'00"
30"
-37°13'00"
30"
3h22m46s
44s
42s
40s
38s
36s